HiSST: International Conference on
High-Speed Vehicle Science Technology
26–29 November 2018, Moscow, Russia

Micro-Aerothermodynamic Analysis of Protuberances and Clearances on a Hypersonic Glider Using a Reduced Domain Approach

Rishabh Choudhury[1,2], Victor F. Villace[3], Johan Steelant[3],
David Buttsworth[4], Marco Marini[5] and Sara Di Benedetto[5]

Abstract

An aerothermodynamic analysis was carried out for the HEXAFLY-INT hypersonic glider incorporating geometrical elements such as wing-aileron gap, aileron hinge cavities, and communication antennas. These features exhibited localised changes to the flow-field affecting local heat-transfer distribution and control surface efficiency as compared to the existing "clean" aerodynamic (AEDB) model. The methodology presented in this paper is based on a reduced flow field domain to study the wing-aileron region and telecommunication antennas of the flight vehicle in more detail by adding the necessary geometrical complexities to the numerical model, while minimising the associated computational costs. This methodology was verified through a comparison with the full domain simulations at cruise fight conditions of the aerodynamic model. Although the aerodynamic coefficients or hinge moments are from a global perspective not severely altered by the presence of openings or cavities, the local heat transfer rates are higher for the detailed model. Modifications to the original flight configuration were suggested that minimise the heat-transfer rates and create a flow field closer to the aerodynamic model.

Keywords: *hypersonics, HEXAFLY, CFD, gap-flows, heat-transfer*

Nomenclature

AEDB	Aerodynamic Database
AoA	Angle of Attack
CMC	Ceramic Matrix Composites
CX	Drag coefficient
CY	Side force coefficient
CZ	Lift coefficient
CM_x	Rolling moment coefficient
CM_y	Pitching moment coefficient
CM_z	Yawing moment coefficient
EFTV	Experimental Flight Test Vehicle
FMM	Flight Modified Model
FOM	Flight Original Model
RANS	Reynolds Averaged Navier-Stokes

α - pitch angle
β - roll angle
ψ - yaw angle
δ - aileron deflection $[^0]$

1. Introduction

The presence of discontinuities and gaps on the external surface of a hypersonic flight vehicle, especially in the region of control surfaces, can result in high heat loads and decrease of the performance and efficiency of the control surfaces. The numerical Aerodynamic Data Base (AEDB) for the HEXAFLY-INT glider was generated by using a nominal "clean" aerodynamic model [1, 2]. The latest status of the HEXAFLY-INT project is presented in more detail in reference [3]. It is important to quantify the

---

[1] *International Research Fellow, ESA-ESTEC, Aerothermodynamics and Propulsion Analysis Section TEC-MPA, Noordwijk, The Netherlands, rishabh.choudhury@esa.int*

[2] *Research Fellow, University of Southern Queensland, Computational Engineering and Science Research Centre, Toowoomba, Australia, rishabh.choudhury@usq.edu.au*

[3] *Research Engineer, ESA-ESTEC, Aerothermodynamics and Propulsion Analysis Section TEC-MPA, Noordwijk, The Netherlands, victor.villace@esa.int, Johan.Steelant@esa.int*

[4] *Professor, University of Southern Queensland, Computational Engineering and Science Research Centre, Toowoomba, Australia, david.buttsworth@usq.edu.au*

[5] *Senior Researcher, Centro Italiano Ricerche Aerospaziali (CIRA), Via Maiorise 81043, Capua (CE), Italy, m.marini@cira.it, s.dibenedetto@cira.it*

variations arising due to differences between the geometrical configuration of the real flight vehicle and the idealised numerical model. These differences have not been considered for the AEDB generation till date, and they have the potential to alter the predicted vehicle characteristics due to the change in the external aerothermodynamics. A Computer-Aided Design (CAD) model of the HEXAFLY-INT hypersonic glider is shown in **Figure** 1. This figure highlights the region of interest for the analysis. The zoomed-in tiles show the detail and complexity that will modelled in the numerical analysis outlined in this paper. The gap present along the wing-aileron hinge line is expected to introduce some "sneak flow" towards the torsion bar cavity in addition to adverse pressure gradients on the external flow. This cavity contains the bearing for the aileron/torsion bar assembly and it is critical to allow actuation of the control surface. Thus, it is important to characterise the flow-field inside the cavity to be able to predict the bearing and surrounding wall temperature during cruise flight conditions.

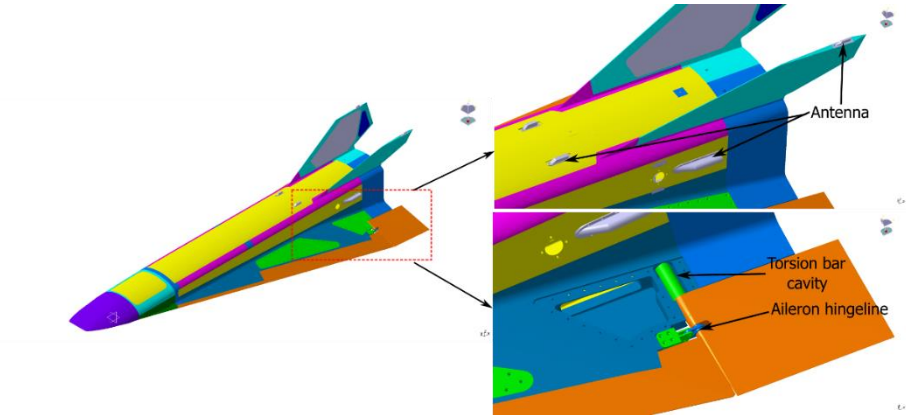

Figure 1. CAD model of the HEXAFLY-EFTV showing the relevant features on the rear of the glider

The numerical analysis of the full glider model including the geometrical details of the wing-aileron region discussed in the previous section would make the computational costs quite high. To reduce computational costs and to study the wing-aileron part of the vehicle in more detail, only the rear section of the vehicle was modelled for the computations undertaken in this work. This is done by imposing an upstream boundary condition interpolated from the numerical analysis of the full nominal model of the glider. The existing aerodynamic model did not include the discontinuities or gaps near the wing-aileron section in order to reduce the computational cost required to populate the large aerodynamic database.

2. Methodology

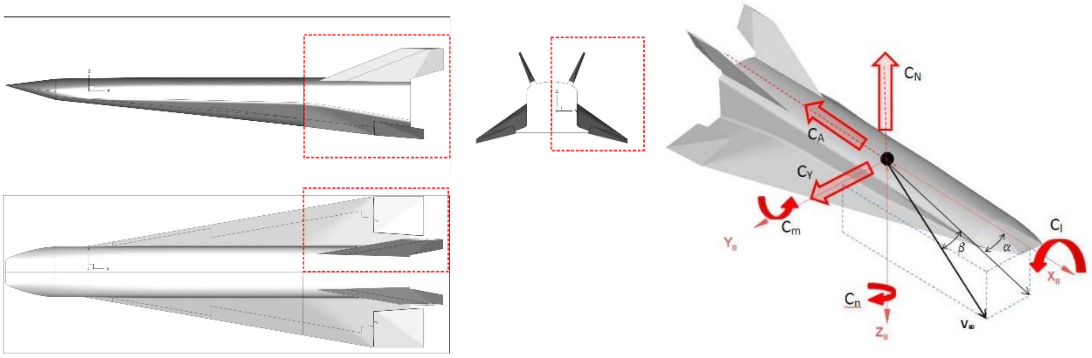

Figure 2. Geometrical section used for detailed numerical analysis highlighted by dashed lines (left) and reference axes used for the setup and analysis of the EFTV vehicle (right).

Figure 2 illustrates the domain that was used for the initial verification of the methodology. From here on, this domain is referred to as the split domain. The current domain was used to only simulate flow conditions where the roll (β) and yaw (ψ) angle of the vehicle are set at zero degrees, exploiting the convenience of a symmetry boundary condition. Nonetheless, this methodology has potential to be extended to various pitch (α), β and ψ angles with the imposed boundary conditions interpolated from the corresponding complete aerodynamic model simulations.

A thorough verification of the current approach was carried out through a numerical analysis on the split domain without the complex geometrical configuration of the real flight vehicle by comparing the results to the full domain computations. Figure 3 shows this split domain along with the imposed boundary condition at the inlet interpolated from the corresponding full domain simulation. Ideally, the numerical results of the split domain computations should be identical to the full domain computations. The flow variables that were interpolated from the full domain simulations to the inlet boundary condition are pressure, velocity vector, density and viscosity.

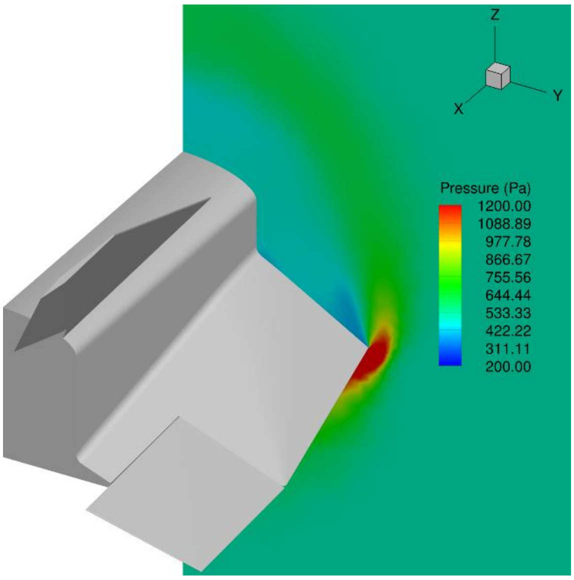

Figure 3. Split model of the EFTV and an example of the imposed dirichlet boundary condition interpolated from the full domain solution.

A hybrid computational grid was generated for the present simulations using the mesh generation software CENTAUR12.0. Several layers of prismatic elements were created at the wall surface to correctly calculate the turbulent boundary layer. The first cell height normal to the wall was set to 10µm to realise a y^+ value below one for the turbulent simulations.

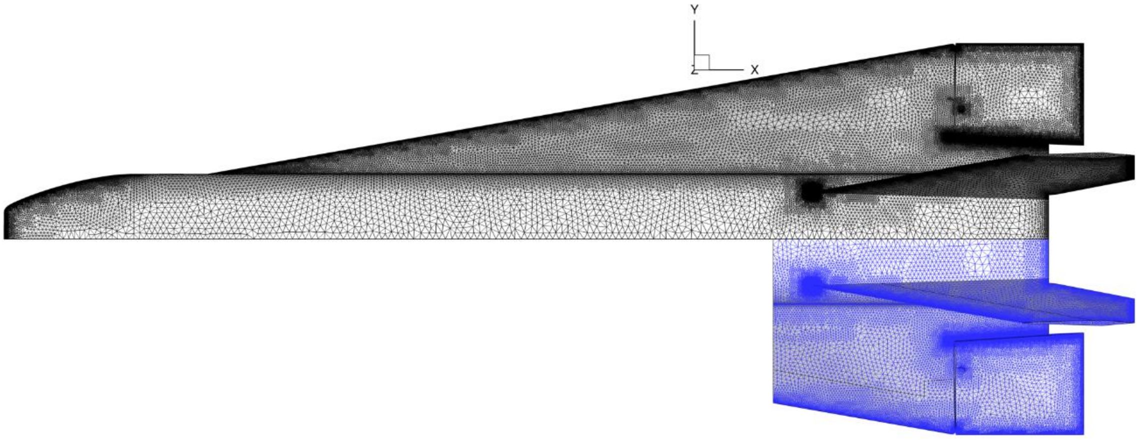

Figure 4. Comparison of the numerical surface grid used for the full (black) and split (blue) domain simulations.

To reduce the impact of the numerical error during the verification process the mesh of the split domain maintained the same mesh generation parameters as the full domain mesh. A comparison of the two surface meshes is shown in Figure 4. It can be observed that the mesh generated for the split domain simulations is similar to the corresponding area of the full domain case. The same clustering of the surface elements is applied to both cases as well the same first cell height and stretching factor for all the mesh elements. The overall cell count for the split domain case was around 6 million cell elements.

The full and split domain simulations were performed using the DLR TAU code [4]. The air thermal and transport properties were computed under the assumption of chemical equilibrium with five species, namely N2, O2, NO, N and O. A second-order upwind AUSMDV scheme by Wada and Liou [5] with a shock fix to prevent the carbuncle phenomenon was used to discretize the fluxes in the Navier-Stokes equations and the eddy viscosity model. A least-square reconstruction of the gradients is used, which provides more accurate results in the presence of hybrid grids. Finally, the RANS equations were integrated towards the steady solution by means of a backward Euler time-relaxation scheme.

The default Spalart and Allmaras [6] model was used for the turbulent closure of the RANS equations. The eddy-to-laminar viscosity ratio was set to 0.1 at the far-field and inflow boundaries. The wall boundary condition is set to a radiative-equilibrium condition with a surface emissivity of 0.4. The freestream conditions used for the computational analysis is set at the nominal cruise condition of the glider: Mach number 7.5, freestream density of 0.007 kg/m^3 and freestream temperature 239.14 K, corresponding to an approximate altitude of 36 km.

3. Verification Analysis

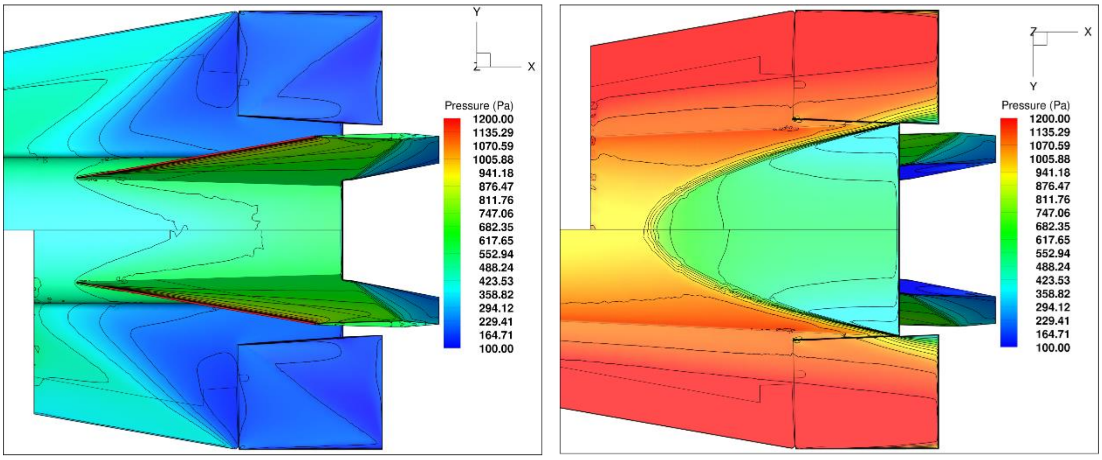

(a) **(b)**

Figure 5. Comparison of the surface pressure distribution between the full and split domain analysis, (a) Leeward Side and (b) Windward Side.

The computational results for both the full and split domain simulations are presented in this section. A comparison of the surface pressure distribution for the two cases is shown in Figure 5 for the leeward and windward side. The overall pressure distribution of the rear of the full vehicle is replicated quite closely in the split domain case. There are some differences which are concentrated on the inlet plane. This is due to the interpolation of the Dirichlet boundary plane from the full vehicle simulations. The first mesh element contributes to this difference in the results. A finer starting cell size at the inlet boundary plane for the split domain case is expected to mitigate this difference.

Figure 6 shows the comparison of the normalized pressure plot along the symmetry of the vehicle and along the aileron centreline. The surface pressure is normalised with respect to the freestream static pressure. The maximum difference in the pressure data between the two sets of simulation is less than 1 percent. The pressure data in the plots are presented for both the leeward and windward side of the vehicle. Figure 7 shows the comparison of the radiative-equilibrium temperature between the full and split domain case. Again, the overall temperature distribution for the split domain case is similar to the full domain simulations in the region of interest. Although, the temperature distribution on the windward side of the vehicle for the split domain case exhibits some differences when compared to the full domain results. Again, these small differences are clustered near the inlet boundary plane for the split domain case. This spurious solution fades out quickly downstream of the inlet plane and does not affect the region of interest.

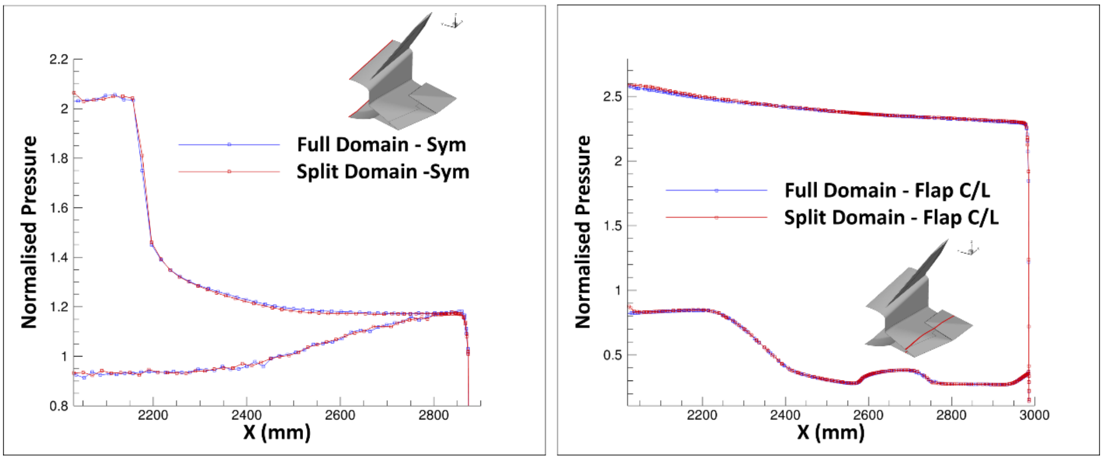

(a) **(b)**

Figure 6. Normalised pressure (P/P∞) plot for full and split domain, (a) at symmetry plane and (b) at the aileron centreline.

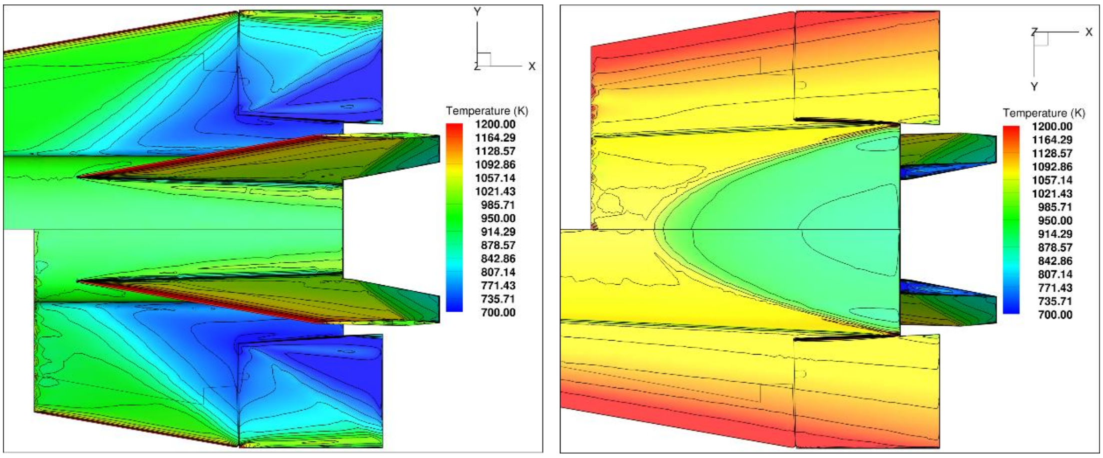

(a) **(b)**

Figure 7. Comparison of the surface temperature distribution between the full and split domain analysis, (a) Leeward Side and (b) Windward Side.

The temperature plots along the symmetry and the centreline of the full and the split domain case are compared in Figure 8 on both the leeward and windward side of the vehicle. The wall temperature is normalised with respect to the total temperature for the cruise flow conditions. This plot is analogous to the plot presented in Figure 6. A comparison of Figure 6 and Figure 8 shows that the surface temperature profile is more susceptible to the split domain approach than the pressure profile immediately downstream of the inlet plane. The temperature profile for the split domain case approaches the surface temperature values for the full domain case within a distance of roughly 150-200mm from the inlet/dirichlet boundary plane. The maximum difference between the full and split domain case for the temperature profile is around 3.5 percent. The influence of this discrepancy in the final vehicle analysis can be reduced by splitting domain further upstream of the area of interest. As is shown by the plot in Figure 8, an upstream distance of roughly 250mm-300mm form the start of the region of interest should be enough to mitigate this difference.

The other objective of the verification analysis is to quantify the effect of the split domain approach on the aerodynamic characterisation of the flight vehicle. This can be quantified by comparing the force and moment coefficients from the full and split domain results. Figure 9 shows the body panels that were chosen as a benchmark for comparison. The aileron is not affected by the split domain approach (un-split panel), whereas the wing panel is split through the reduced domain as seen in Figure 9(b). The differences in the force and moment coefficients for these panels along the X, Y and Z axes respective to the vehicle body are presented in Table 1.

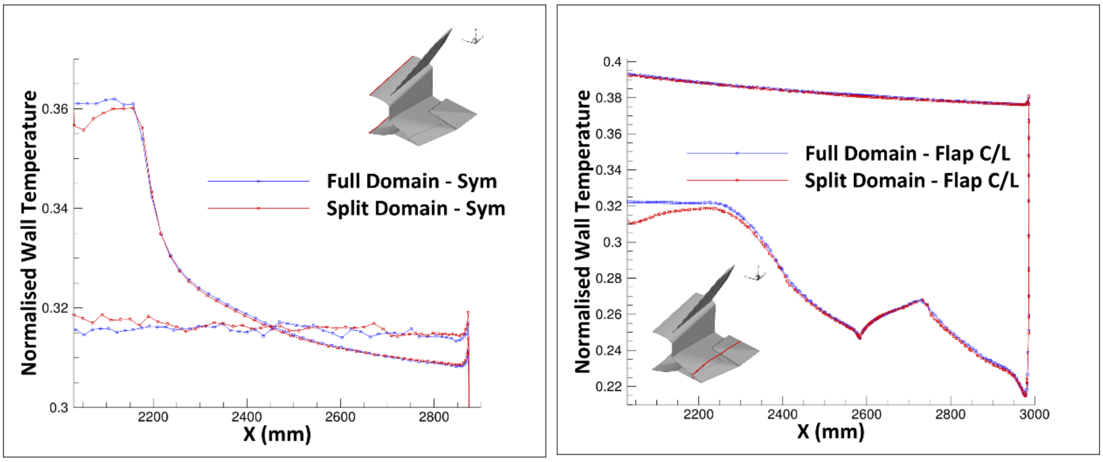

(a) **(b)**

Figure 8. Normalised temperature (T/T₀) plot for full and split domain, (a) at symmetry plane and (b) at the aileron centreline.

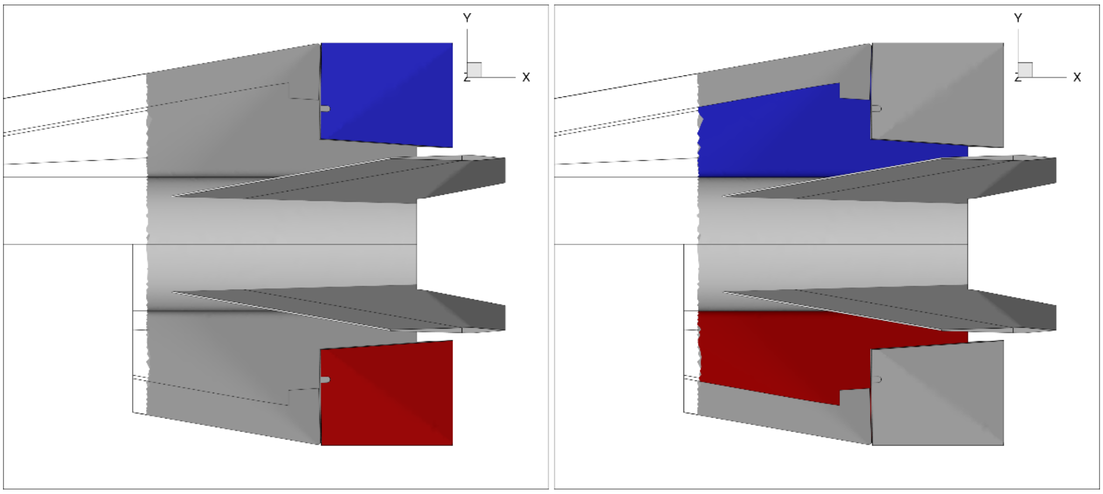

(a) **(b)**

Figure 9. Panels selected for comparison of force and moment coefficients. (a) Un-split aileron panel, and (b) Split wing panel. Blue - Full domain results, Red - Split domain results.

The difference in the aerodynamic coefficients between the full and split domain simulations for the two selected panels is less than 0.5%. This further validates the reduced domain modelling approach. Moreover, it should be noted that the force and moment data presented for the split panel (wing panel) were integrated as from 50 mm downstream of the inlet plane. This eliminates the spurious solution near the Dirichlet boundary condition.

Table 1. Difference in the force and moment coefficients between the full and split domain simulations for both panels.

	Aileron Panel (Un-split)	**Wing Panel (Split)**
	Difference (%)	Difference (%)
Moment Coefficients		
CM_x	0.18	0.01
CM_y	0.16	0.05
CM_z	0.24	0.01
Force Coefficients		
C_x	0.01	0.29
C_y	0.21	0.01
C_z	0.17	0.05

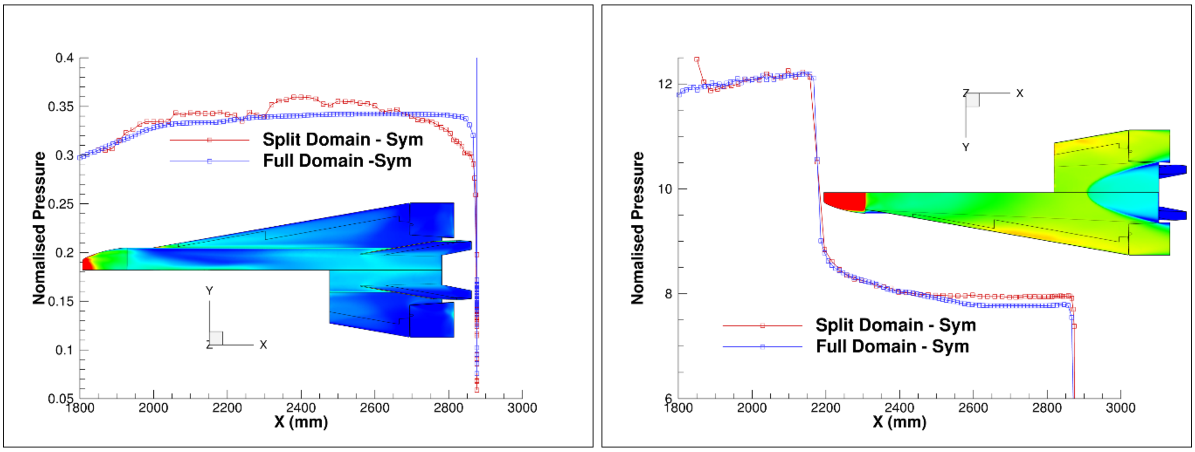

Figure 10: Normalised pressure (P/P∞) plot for full and split domain at symmetry plane for the top (left) and bottom (right) surface at AoA = 15^0 and Mach 7.5.

Verification analysis for the reduced domain methodology was also conducted at AoA of 15^0 and 5^0 for the EFTV. The analysis was carried out to quantify the sensitivity of the methodology to AoA of the EFTV. Figure 10 and Figure 11 plot the surface pressure distribution along the symmetry plane for both the full and split domain. The mismatch in the pressure data between the split and full domain model for AoA 15^0 on the leeward (top) and windward (bottom) side is around 6% and 3%, respectively. Similarly, the difference in the pressure data for AoA -5^0 on the leeward (bottom) and windward (top) is around 2% and 4.5%, respectively.

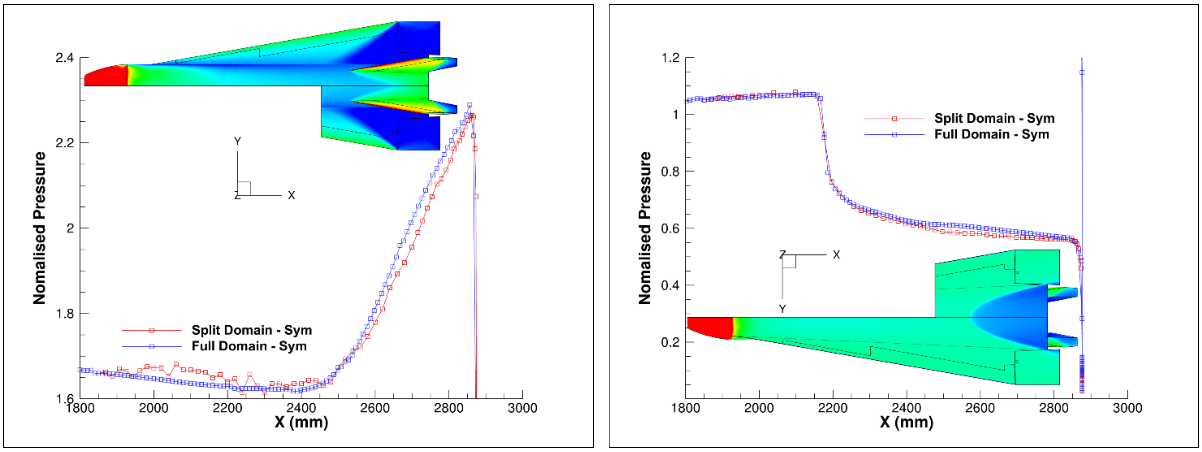

Figure 11: Normalised pressure (P/P∞) plot for full and split domain at symmetry plane for the top (left) and bottom (right) surface at AoA = -5^0 and Mach 7.5.

This analysis shows that the reduced domain methodology is sensitive to the AoA and the region of interest on the EFTV, i.e. either windward or leeward side. Additionally, a higher AoA results in a greater discrepancy between the full and split domain results. The effect of this discrepancy on the aerodynamic coefficients of a split panel was analysed using the same methodology presented in Table 1. The maximum difference in the aerodynamic coefficients between the full domain case and the split-domain approach for the split-panel is around 2.8% for an EFTV AoA of 15^0.

4. Micro-Aerothermodynamics on Detailed Configuration

The previous section outlined the numerical procedure that was undertaken to verify the feasibility of the split domain approach. This section incorporates to the numerical analysis the geometrical features representative of the final flight vehicle design. Figure 12 highlights these additional geometrical features. The wing-aileron gap was resolved in the aerodynamic model as well as the current detailed analysis.

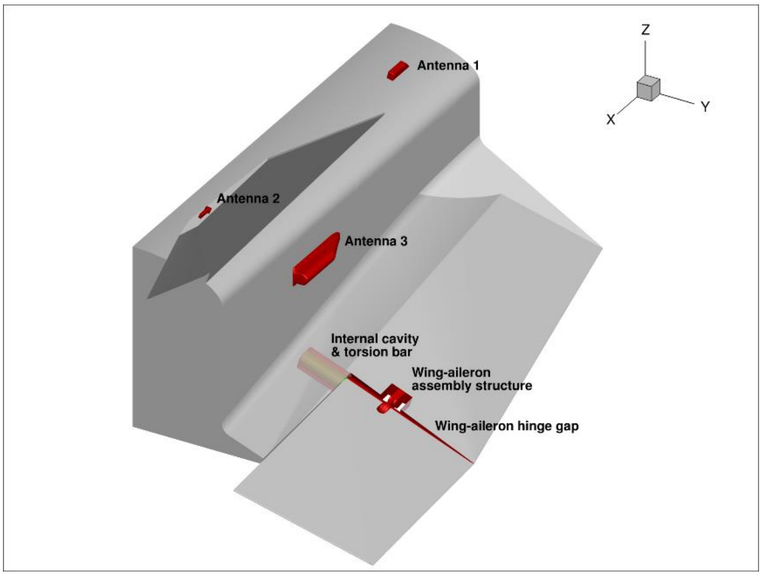

Figure 12: Original flight configuration highlighting the additional geometrical detail incorporated compared to the clean AEDB model.

The temperature distribution along the leeward side of the detailed numerical model, in Figure 13, highlights the effect of the wing-aileron gap and cavity on the control surface. The initial results show the presence of a horse-shoe vortex type flow feature on leeward side of the control surface, thereby affecting the pressure distribution on the aileron surface.

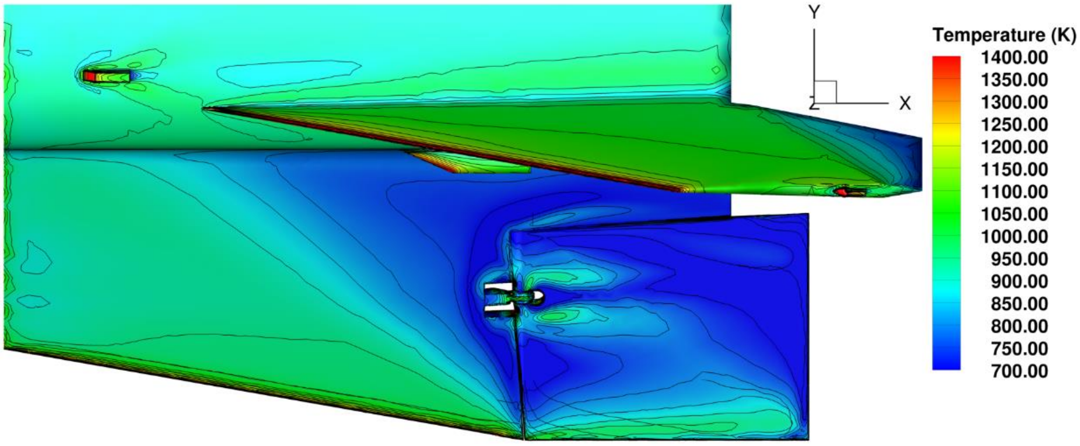

Figure 13: Temperature distribution on the leeward side for the detailed numerical model.

Figure 14 shows the Mach number contours on a cut-plane across the aileron-wing hinge cavities. The high-pressure flow from the windward surface of the vehicle leaks through the hinge cavity to the leeward side boundary layer, thus generating the hot region downstream seen in Figure 13. Due to the pressure difference between windward and leeward sides, the jet through the hinge cavities becomes supersonic, as shown by the Mach number distribution. Figure 15 shows the temperature distribution on the windward side of the vehicle and highlights the temperature distribution due to the presence of the wing-aileron assembly structure. The higher temperatures observed around this section of the vehicle are due to the presence of the wing cavity as well the assembly structure marginally protruding out on to the oncoming flow.

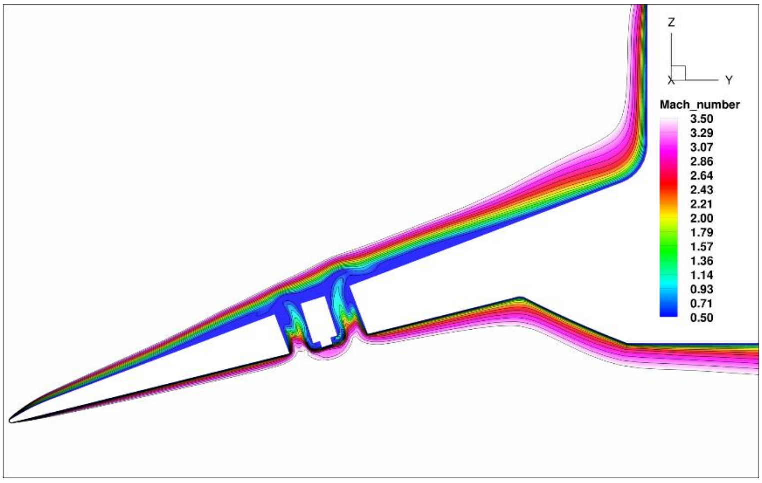

Figure 14. Slice of the numerical model showing the influence of the windward pressure on the leeward side due to the wing cavity.

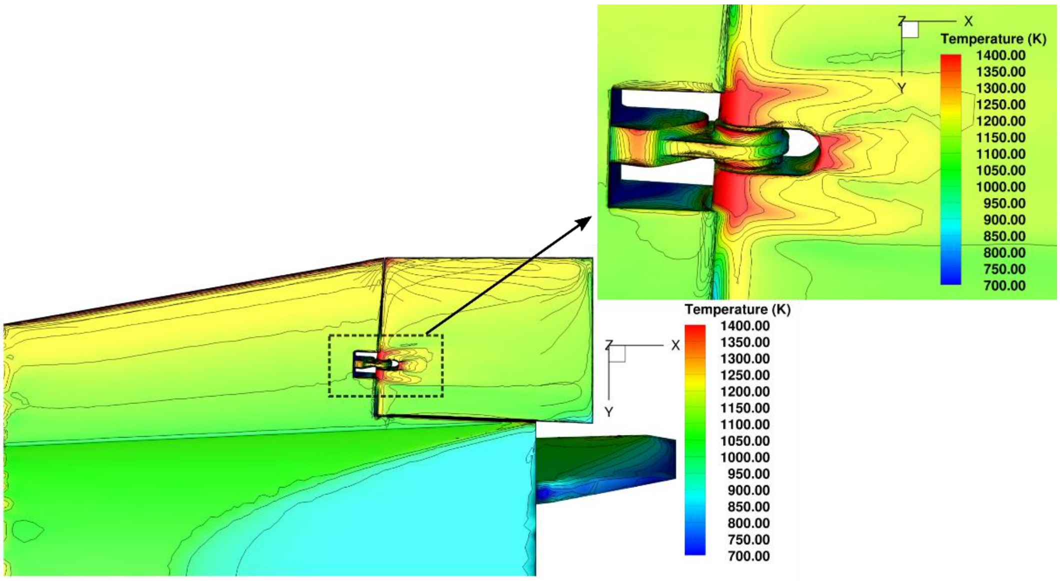

Figure 15. Temperature distribution on the windward side along with hinge detail.

The temperature distribution of the torsion bar cavity is shown in Figure 16. The objective of the simulations was to quantify the convective heating and cross-flow into the torsion bar cavity during the hypersonic flight. The bearing at the end of the torsion bar assembly is a critical component for the flight mission. Hence, it is important to assess the effect of the flow on the torsion bar assembly. Figure 16 shows that even though high temperatures are expected at the start of the torsion bar cavity the effect of convective heat-transfer is minimal at the end of the cavity, where the bearing is located. It should be noted that since the assumption of radiative-equilibrium was used for the wall temperatures in the simulations, the temperatures calculated would be over-estimated w.r.t to the actual wall temperatures during the hypersonic flight. Furthermore, the absence of conjugate heat transfer in the present model is another source of over-estimation of the wall temperature.

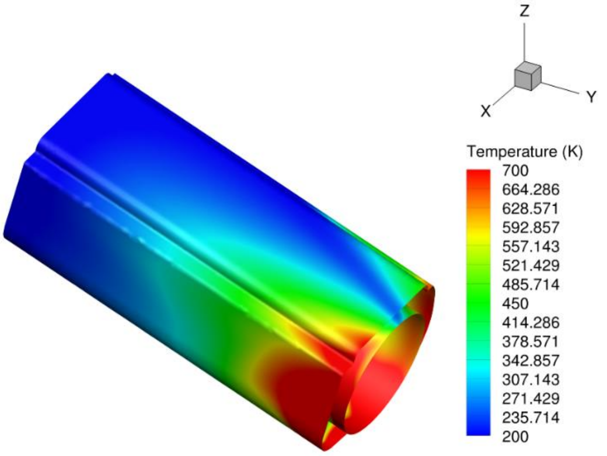

Figure 16: Cavity wall and torsion bar temperature (radiative equilibrium wall).

Figure 17 shows the surface streamlines on the split model for the original flight model on the leeward side. An extended separation zone is observed around the wing cavity for the original flight model. The presence of the hinge line, wing cavity and the aileron cavity introduces a complex flow field at the trailing edge of the wing and over the aileron surface compared to the nominal clean AEDB model.

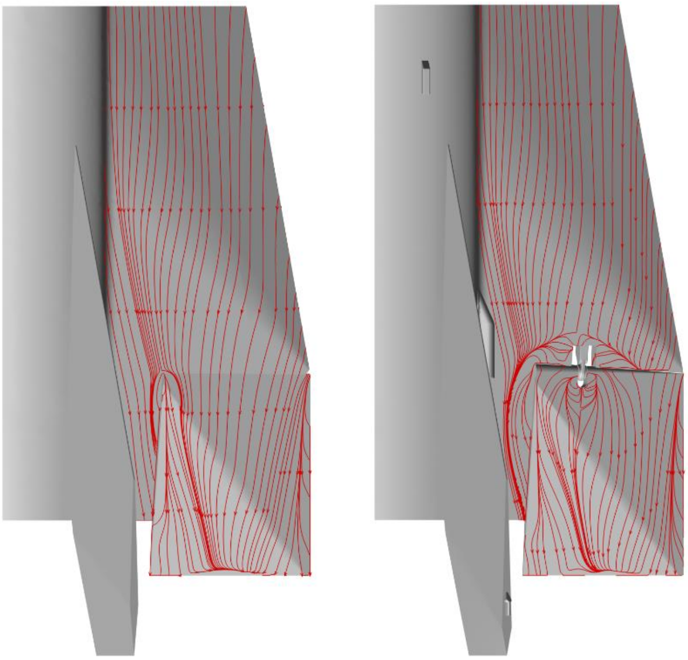

Figure 17: Comparison of surface streamlines between the AEDB (left) and original flight (right) model for AoA = 0^0 and $\delta_{aileron}$ = 0^0.

The additional heating around the wing-aileron hinge line and cavity region shown in Figure 15 necessitated a change in the configuration of the original flight model (FOM), in order to lower the heat-transfer rates and to further minimize the adverse flow field. The changes incorporated to the original flight model (FOM) are detailed in Figure 18. It shows the changes to the wing-aileron region and the CMC aileron itself. The main objective behind the proposed changes is to lower local heating hotspots and improve flow efficiency around the hinge-line region. The wing-cavity section was covered with a closed surface conformal to the outer profile of the wing.

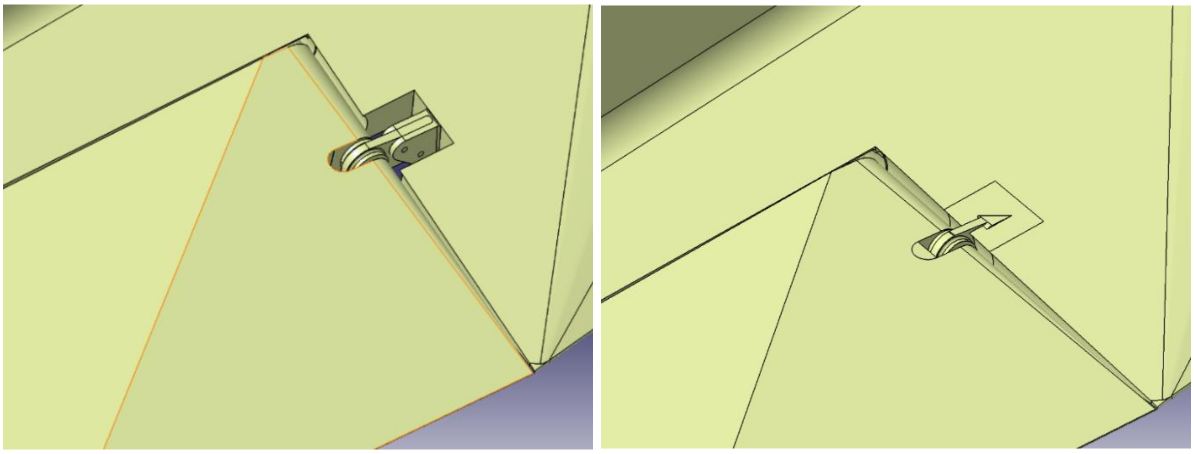

Figure 18: Proposed modifications (right) to the original flight model (left) to reduce adverse flow effects and high heat-transfer regions.

Figure 19 compares the surface streamlines between the flight original model (FOM) and the flight modified model (FMM). The FMM has a smaller recirculation region for the same flow condition compared to the FOM. This is due to the lack of the cavity in the wing, which introduces an adverse pressure gradient in the case of the FOM. Moreover, the size of the recirculation region on the aileron decreases for the FMM compared to the FOM.

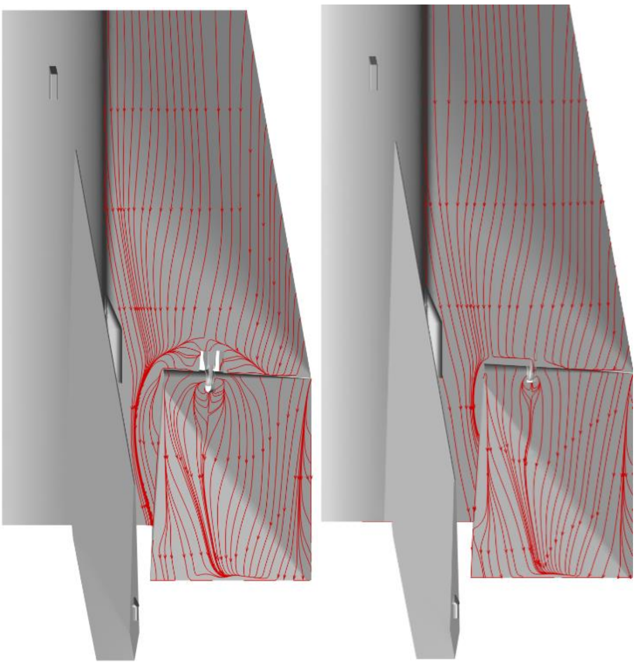

Figure 19: Comparison of surface streamlines between the original flight model (FOM, left) and modified flight model (FMM, right) for AoA = 0^0 and $\delta_{aileron} = 0^0$ at Mach 7.5.

A comparison of the aileron leading edge temperature between the flight original model (FOM) and the modified flight model (FMM) is shown in Figure 20 for both the adiabatic and radiative equilibrium wall condition on the aileron leading edge. The design changes presented in the modified flight model drastically lower the aileron leading edge temperatures compared to the original flight model. The higher temperatures observed in the FOM are due to the presence of the wing cavity which leads to flow stagnation at the aileron leading edge. In the FMM, the cavity is closed up leading to much lower temperatures in the mid-span section of the aileron leading edge. The temperatures on the inboard and outboard part of the aileron leading edge are roughly the same for both the models. This is due to the disturbance in the flow field in the FOM model, mainly concentrated in the mid-section of the aileron hinge line as shown in Figure 19.

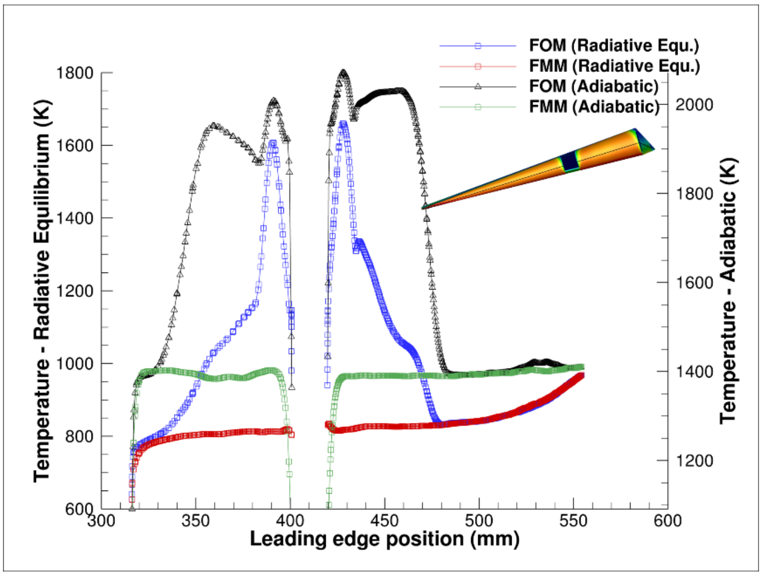

Figure 20: Comparison of the aileron leading edge between the flight original model and the flight modified model for both the adiabatic and radiative equilibrium wall boundary condition, AoA = 0^0 and $\delta_{aileron}$ = 0^0 at Mach 7.5.

A close-up of the heat-transfer distribution at the aileron-wing hinge line is shown in Figure 21. The difference in the heating distribution is mainly due to the presence of the wing and aileron hinge cavity. The difference is present both upstream and downstream of the hinge line. The flow field and the corresponding heat-transfer rate non-uniformity on the aileron wing surface is greater for the original flight model when compared to the modified flight model.

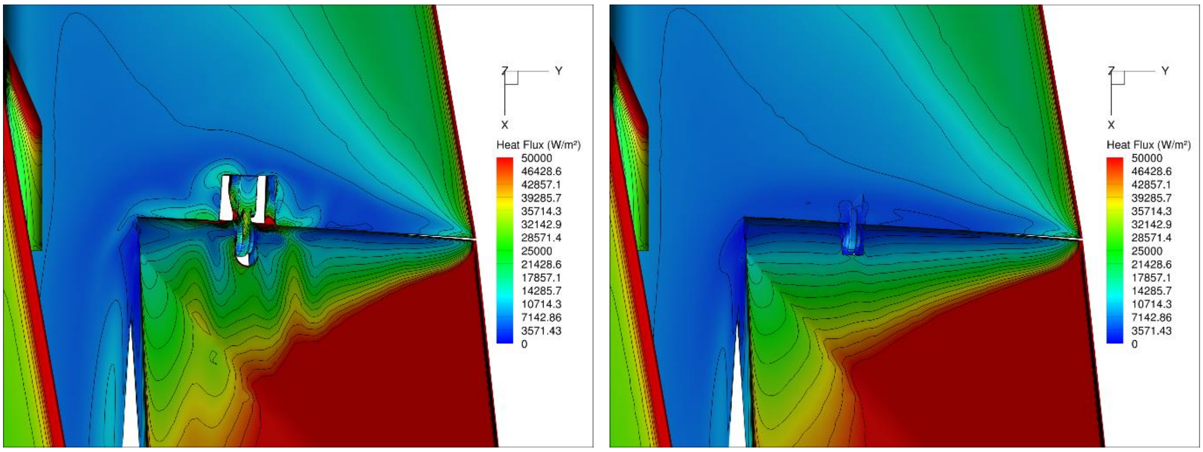

Figure 21: Comparison of wall heat flux on the leeward side of the original (left) and modified flight model (right) for a flap deflection angle of -20^0 and AoA = 0^0 at Mach 7.5 at the wing-aileron hinge line.

The variation on the aerodynamic coefficients of the AEDB model due to the geometrical details, antennas, hinge-line etc., can be evaluated by incorporating these changes in the split model according to the following equations for the generic aerodynamic coefficients:

$$C_x^{total} = C_x^{no\ box} + C_x^{box}$$

$$C_x^{total,\ new} = (C_x^{total} - C_x^{box}) + C_x^{box,\ new}$$

$$\Delta C_x^{total} = C_x^{total,\ new} - C_x^{total}$$

The reference system used for all the aerodynamic coefficient data presented in this work was based on the reference axes shown in Figure 2. The pole co-ordinate around which the moments for the EFTV were calculated are (1.455 m, 0 m, 0.12 m). This pole was chosen as the reference point for all the aerodynamic calculations. The reference area used for the vehicle is 2.52 m^2, and the reference length for rolling/yawing and pitching moment coefficients are 1.24 m and 3.29 m, respectively.

	AEDB Model	**Flight Original Model**		**Flight Modified Model**	
Force Coefficients			Difference (%)		Difference (%)
CX	0.0065687	0.0066206	0.87	0.0066011	0.49
CY	0.0007817	0.0006607	-15.4	0.0006864	-12.2
CZ	0.0196104	0.0194539	-0.79	0.0195175	-0.47
Moment Coefficients					
CM_x	0.004575	0.0045269	-1.05	0.0045545	-0.45
CM_y	-0.000196	-0.0001445	26.6	-0.0001647	15.9
CM_z	0.002436	0.0023212	-4.73	0.0023526	-3.44

Table 2: Difference in aerodynamic coefficients between the AEDB and the flight original and modified configuration at AoA = 0^0 (half vehicle)**.**

The differences in the CY and CM_y between the AEDB and the original and modified flight model shown in Table 2 are due to the presence of the three antennas and the separation region on the wing ahead of the wing-aileron hinge-line. The presence of the antenna shock as shown in Figure 22 contributes to the changes in the lateral force coefficient, CY and the pitching moment coefficient, CM_y between the three configurations. The effects of the separation region is minimised in the proposed modified flight model since the wing cavity is covered and this creates a smaller separation of region as seen in Figure 19, which in turn leads to a smaller difference in the pitching moment coefficient between the modified flight configuration and the AEDB model. It is important to note that the aerodynamic coefficient values and the differences presented in Table 2 are based on the half-EFTV model along with a symmetry boundary condition. Ideally for the full model, the CY, CM_x and CM_z values would be zero due to zero yaw and roll angle, and the CX, CZ and CM_y values would be twice the value presented due to the use of the full vehicle reference area to compute the vehicle aerodynamic coefficients, i.e. 2.52 m^2. Nonetheless, Table 2 presents the differences between all three models and gives us an insight into the effect of the change in flow-field on the aerodynamic characteristics of the vehicle.

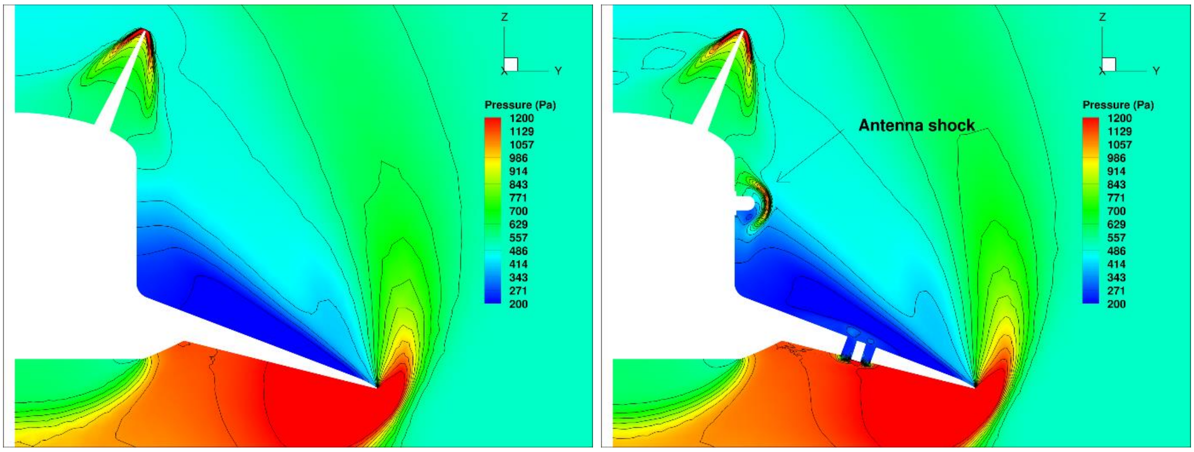

Figure 22: Comparison of the pressure distribution on a slice plane between the AEDB and original flight configuration. Slice location at X= 2540 mm at AoA = 0^0.

Figure 23 shows the surface pressure distribution on the leeward side for the AEDB model and the original flight configuration. The presence of the three antennas changes the pressure distribution creating localised high pressure regions along with changes due to the presence of the wing-aileron hinge gap and the wing-cavity. These changes in the pressure distribution on the leeward side of the vehicle contributes to the differences in the CM_y values between the two different configurations.

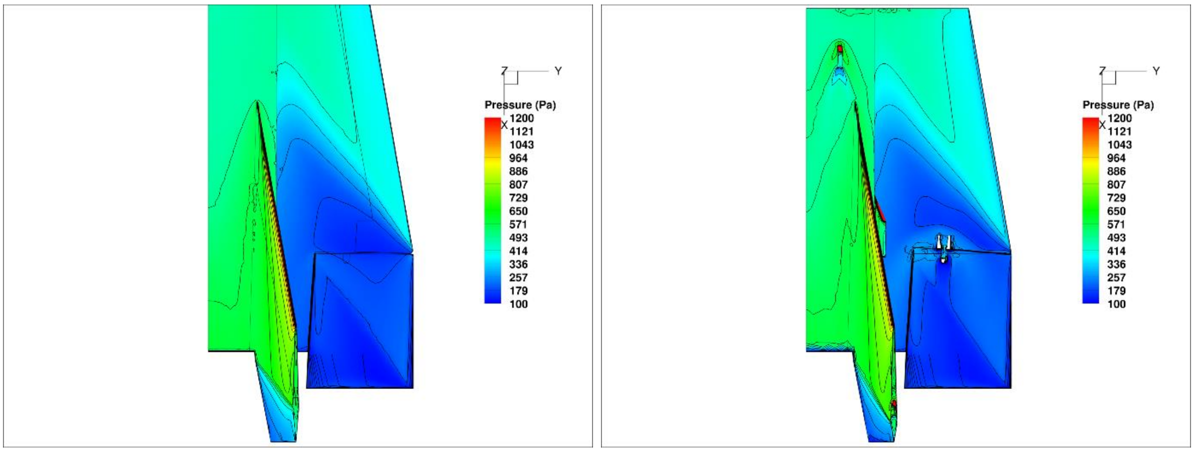

Figure 23: Top view of the leeward side of the AEDB (left) and original flight (right) configuration for an AoA = 0^0 and no flap deflection.

The presence of the hinge-line gap introduces some changes to the flow-field near the wing-aileron region. This is shown in Figure 24 where the high pressure from the windward side of the vehicle penetrates through the hinge-line gap to introduce a supersonic jet injection and a crossflow type interaction on the leeward surface of the wing-hinge region. The supersonic stream of air introduces a boundary layer separation upstream of the hinge-line, as well as near the downstream region on the CMC wing surface. This jet penetration effect is more drastic for the case presented in Figure 24 since the pressure difference between the windward and the leeward surface is one of the maximum out of all the cases studied for this work due to the high angle of attack for the EFTV (AoA = 15^0).

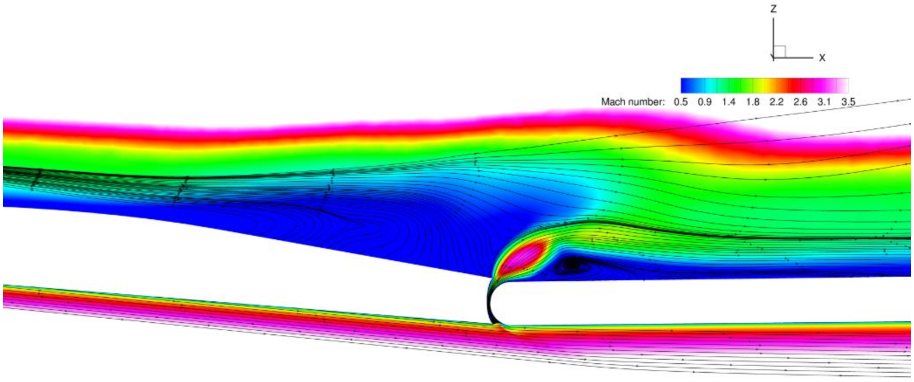

Figure 24: Slice view along the length of the vehicle showing the flow features at the wing-aileron hinge gap, AoA = 15^0 and $\delta_{aileron} = -5^0$.

The difference between the AEDB model and the original flight model (FOM) is further highlighted in Figure 25. This figure compares the flow field along the span of the EFTV for the AEDB model and modified flight model for an AoA of 15^0 and flap deflection of -5^0. The high pressure from the windward surface of the vehicle induces a change of the flow on the leeward side for both the models, but in the case of the modified flight model, the flow on the leeward surface of the EFTV is further disturbed by the presence of the wing cavity and the presence of the hinge-line gap. The supersonic jet penetration effect in this can also be attributed to the presence of the hinge gap on the CMC wing. This effect is analogous to the one seen in Figure 24. As mentioned previously, these changes in the flow-field can lead to a variation in the aerodynamic coefficients and hence, the flight characteristics of the EFTV.

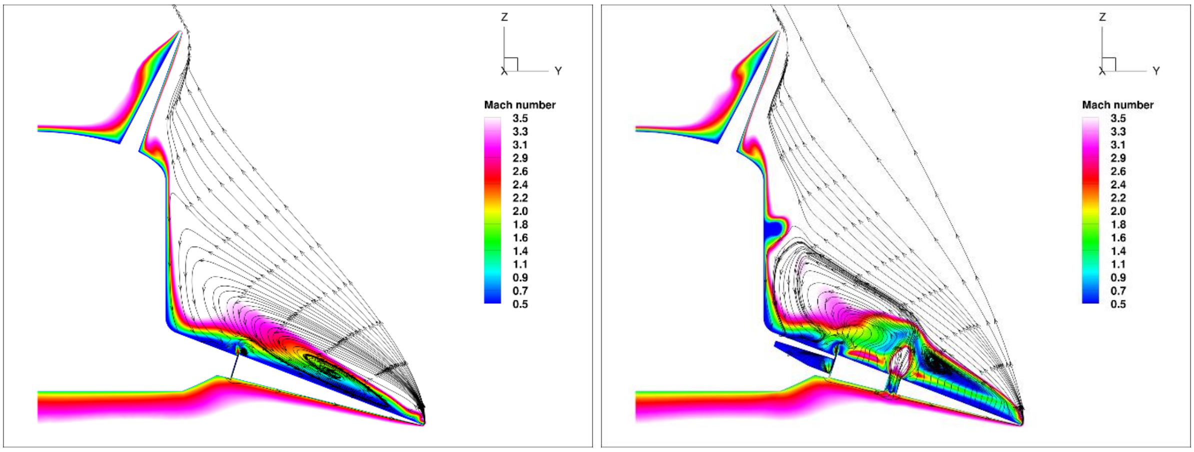

Figure 25: Slice view of the vehicle along the span of the vehicle showing the difference between the flow features of the AEDB and the flight modified configuration AoA = 15^0 and $\delta_{aileron}$ = -5^0.

A further analysis was conducted to characterise the hinge moment coefficients for the aileron of the EFTV due to the changes in the flight model from the nominal AEDB configuration, and to quantify any changes. As mentioned earlier, the presence of the hinge line gap, and wing-aileron assembly cavity changes the pressure distribution on the ailerons of the EFTV. This can induce a change in the hinge moment coefficients for the EFTV and thus it is important to quantify the changes.

Figure 26 shows a comparison of the hinge moment coefficients between original flight model and the modified flight model for different flap angles at an AoA of 0^0. The changes in the hinge moment coefficients is relatively small for the low flap angles but at a larger flap angle of -20^0, the hinge moment coefficient is around 7% higher for the modified flight model. A comparison of the hinge-moment coefficients between the AEDB model and the modified flight model is presented in Figure 27 for AoA of -5^0 and 15^0. The maximum difference is around 4.7% for an AoA = 15^0 and flap deflection = -15^0.

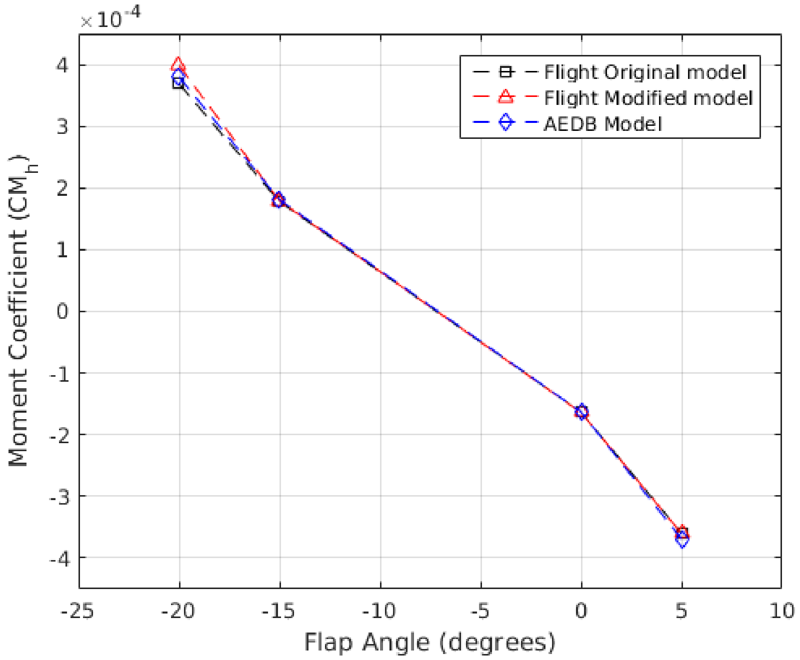

Figure 26: Hinge moment comparison between the original flight and modified flight configuration for different aileron deflection angles for AoA = 0^0.

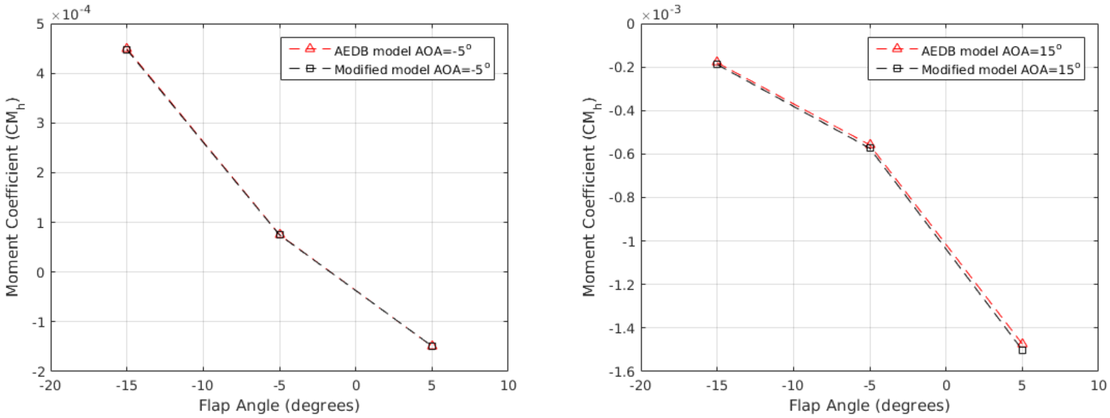

Figure 27: Hinge moment comparison between the AEDB model and the flight modified configuration for the test-matrix cases for AoA = -5^0 (left) and for AoA = 15^0 (right).

Figure 28 outlines a comparison of the Cm_y pitching moment coefficients versus the angle of attack of the full EFTV vehicle between the AEDB and the flight modified model for various aileron deflection angle. This figure shows that the trim characteristics for the EFTV based on the AEDB model is similar to the flight modified model for aileron deflection angle for 5^0 and -5^0. The changes in the trim angle of the EFTV for the aileron deflection angle is around 0.5^0. Although, the trim angle for the vehicle changes by about 2^0 for the aileron deflection of -15^0 between the AEDB and flight modified model. Through the interpolation of this data set, we can calculate the AoA for the trim condition for the aileron deflection cases simulated in this study. These AoAs for the trim conditions are plotted against their corresponding aileron deflection angle in Figure 29.

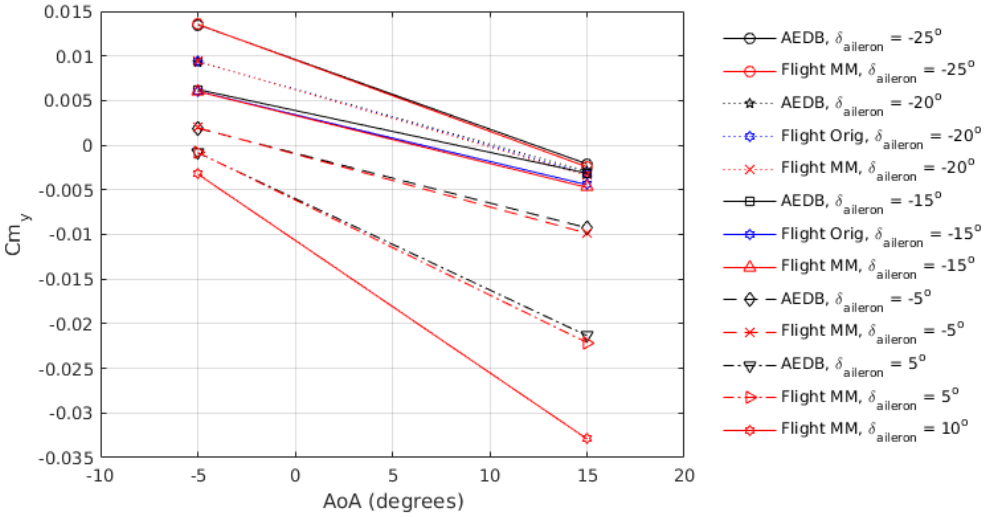

Figure 28: Comparison of pitching moment coefficient for different flap deflection angles between the AEDB model and modified flight model.

Figure 29 plots the aileron deflection angle for the EFTV required to maintain a fixed AoA. The AEDB model shows a non-linear behaviour at high aileron deflection angle between -5^0 and -20^0 compared to the linear behaviour of the modified flight model even at higher aileron deflection angle. This is possibly because the AEDB model predicts a larger separation region on the windward side of the aileron compared to the modified model. The presence of the hinge-line in this case leads to a more efficient flow field for the modified flight model, with a smaller separation region at the wing-aileron region (compression corner) and over the aileron itself. Although, this leads to a lower flap efficiency due to spillage through the hinge line.

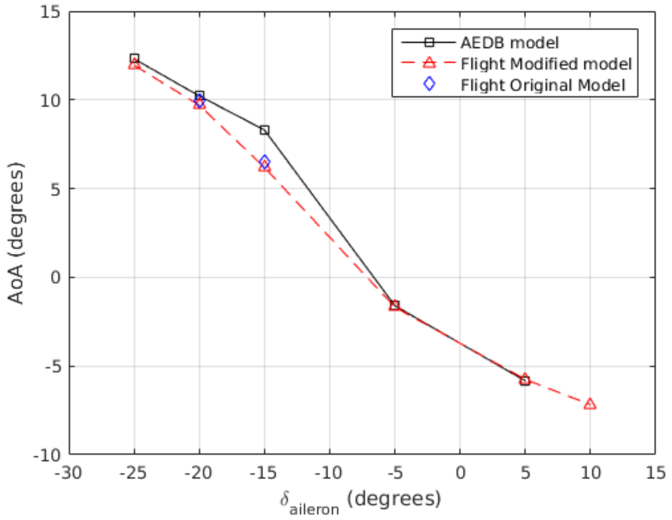

Figure 29: $\delta_{aileron}$ deflection required to maintain a fixed AoA.

This difference in the flow field is shown in Figure 30 where the AEDB flow field is represented by blue streamlines and the modified flight model is represented by red streamlines for $\delta_{aileron}$ = -15^0 and AoA = -5^0. The trim AoAs for the $\delta_{aileron}$ = -15^0 based on the AEDB and modified flight model are 8.3^0 and 6.2^0 respectively, i.e. a difference of 2.1^0. Overall, the presence of the hinge line on the flight modified model reduces the aileron efficiency at higher aileron deflection angles compared to the AEDB model as shown in Figure 29. Although, the trim angles for higher aileron deflection angles approaches the AEDB values, possibly indicating that there might be a crossover point for the flap efficiency between the AEDB and flight modified model for $\delta_{aileron}$ > -25^0, i.e. higher than 25^0 flaps up.

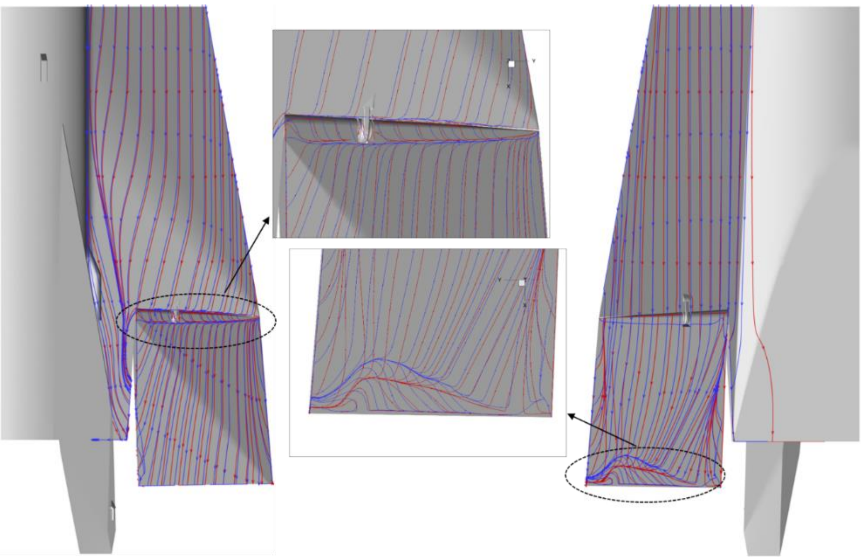

Figure 30: Comparison of the overlaid streamlines between the AEDB (blue) and flight modified model (red) on the leeward and windward side of the EFTV at AoA = -5^0 and $\delta_{aileron}$ = -15^0.

Another geometrical feature investigated as a part of the current analysis is the thermal state of the torsion-bar cavity which contains the torsion-bar bearing. The torsion-bar bearing is an integral part of the aileron deflection mechanism during flight, hence in it is important to analyse the effect of any "sneak" flow into the cavity chamber during flight which can have a detrimental effect on its performance. The simulation for AoA = 0^0 and $\delta_{aileron}$ = 0^0 for the FOM and FMM configurations were conducted using both the radiative equilibrium and adiabatic wall conditions for a comparison of the wall temperatures. These two wall conditions over estimate the wall temperature due to the lack of conjugate heat-transfer analysis in the CFD model but nonetheless it is useful to provide a conservative estimate of the torsion bar bearing wall temperature. The adiabatic wall temperature at the torsion bar bearing is around 100 K higher than the radiative equilibrium wall condition case as shown in Figure

31(a). The large separated region in the FOM compared to the FMM configuration, leads to higher torsion bar cavity wall temperatures for the FOM configuration for both the radiative equilibrium and adiabatic wall boundary condition cases.

Figure 31(b) shows the temperature distribution on the torsion-bar cavity wall and torsion-bar wall for the EFTV at 0^0 AoA at Mach 7.5 for both the original flight model and modified model. All cases show that the temperature on the torsion-bar bearing due to convective heating is below the bearing maximum operating temperature of around 500 K. Moreover, the effect of convective heat-transfer is minimal at the end of the cavity, where the bearing is located. It should be noted that since the assumption of radiative-equilibrium was used for the wall temperatures in the simulations, the temperatures calculated would be over-estimated to the actual wall temperatures during the hypersonic flight. Furthermore, the absence of conjugate heat transfer in the present model is another source of over-estimation of the wall temperature.

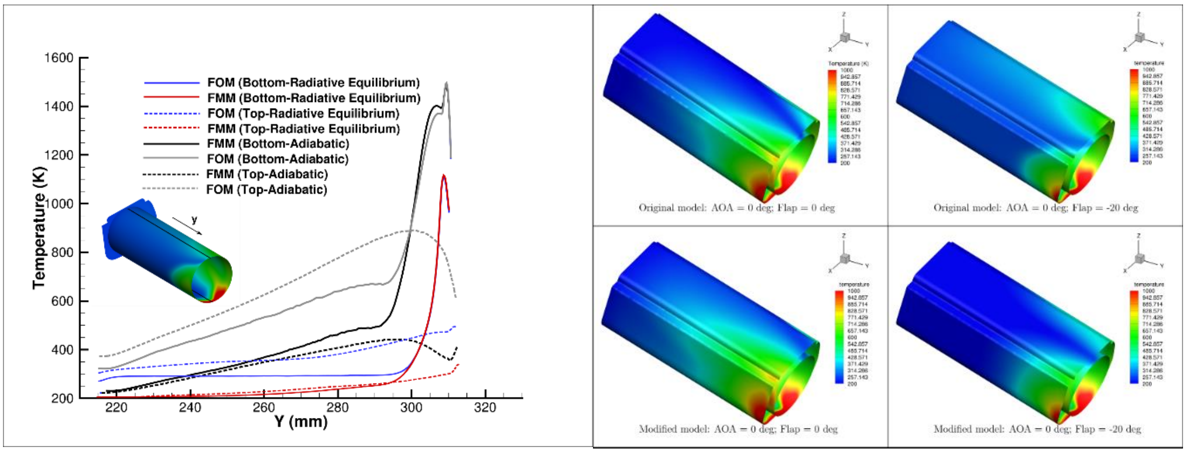

(a) (b)

Figure 31: (a) Temperature profile along the torsion bar length for the top and bottom surface, (b) Temperature distribution for the torsion bar cavity; AoA = 0^0 and $\delta_{\text{aileron}} = 0^0$ and Mach 7.5

The internal cavity temperature, velocity magnitude and the streamlines for the FOM at AoA = 0^0 and $\delta_{\text{aileron}} = 0^0$, FMM at AoA =$0^0$ and $\delta_{\text{aileron}} = 0^0$ and FMM at AoA =15^0 and $\delta_{\text{aileron}} = 5^0$ are shown in Figure 32, Figure 33 and Figure 34 respectively. The temperature and velocity magnitude plots gives an idea on the amount of "sneak flow" inside the torsion-bar cavity for the three different configuration. The large flow separation on the leeside of the EFTV at AoA = 15^0 leads to a higher volume of internal flow and thus leading to higher torsion bar temperature. The maximum temperature for the torsion bar is shown to be close to 500 K for AoA=15^0 and $\delta_{\text{aileron}} = 5^0$. This is near the maximum operating temperature of the torsion bar bearing. Hence, for the flight tests the torsion bar cavity will be packed with a foam-type porous material to reduce the convective heat transfer rates to the torsion bar bearing. Again, it is important to note that the current simulations overestimate the wall temperatures due to the absence of conductive heat-transfer.

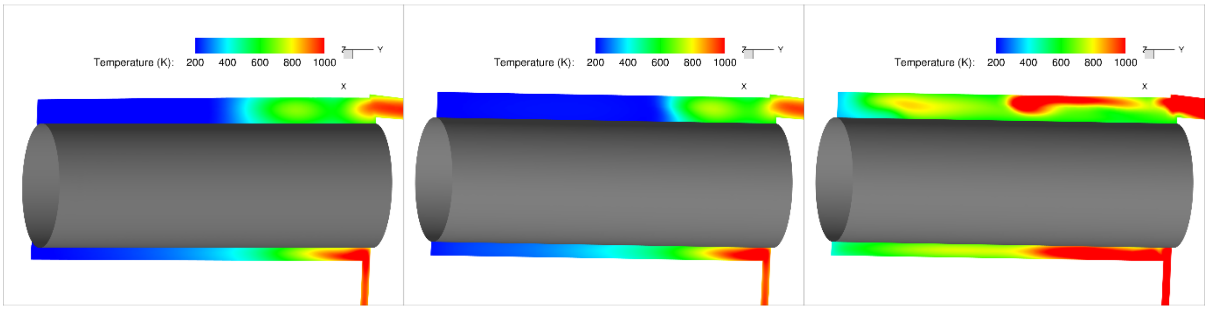

(a) (b) (c)

Figure 32: Internal torsion-bar cavity temperature at Mach 7.5, (a) FOM, AoA = 0^0, $\delta_{\text{aileron}} = 0^0$ (b) FMM, AoA = 0^0, $\delta_{\text{aileron}} = 0^0$, and (c) FOM, AoA = 15^0, $\delta_{\text{aileron}} = 5^0$.

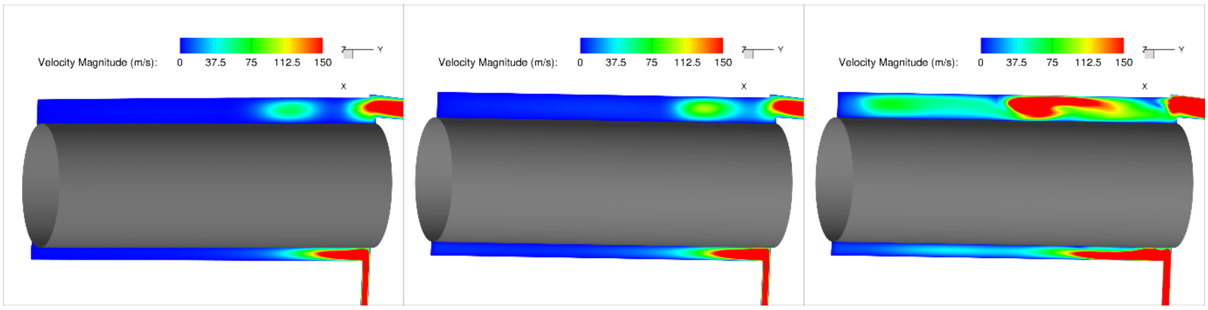

(a) (b) (c)

Figure 33: Internal torsion-bar cavity velocity magnitude at Mach 7.5, (a) FOM, AoA = 0^0, $\delta_{aileron}$ = 0^0 (b) FMM, AoA = 0^0, $\delta_{aileron}$ = 0^0, and (c) FOM, AoA = 15^0, $\delta_{aileron}$ = 5^0.

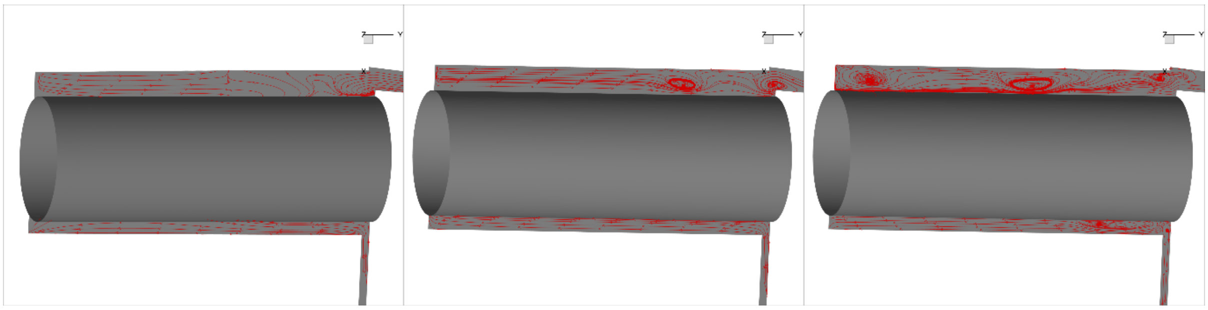

(a) (b) (c)

Figure 34: Internal torsion-bar cavity streamlines at Mach 7.5, (a) FOM, AoA = 0^0, $\delta_{aileron}$ = 0^0 (b) FMM, AoA = 0^0, $\delta_{aileron}$ = 0^0, and (c) FOM, AoA = 15^0, $\delta_{aileron}$ = 5^0.

5. Conclusions

An aerothermodynamic analysis of the detailed configuration of the EFTV flight model was carried out based on a split computational domain approach using the DLR TAU code. The detailed configuration of the EFTV model included the presence of the wing-aileron hinge-line gap, wing-cavity gap, torsion-bar cavity and external antennas. The split domain approach was used to reduce the computational costs associated with the detailed simulations. The main aim of the study was to quantify the effect of the additional geometrical details on the EFTV, and to compare the aerodynamic characteristics of the detailed model to the computations performed using the "clean" model defined for the aerodynamic database of the EFTV.

Firstly, the spilt-domain computational methodology was verified by performing a numerical analysis on the split domain without the complex geometrical configuration of the real flight vehicle and by comparing the results to the full domain computations. These verification simulations showed that the split-domain approach was able to reproduce the pressure and temperature distributions close to values observed on the full domain simulations. The temperature distribution data was sensitive to the initial boundary plane of the split domain model, hence a length of 300 mm upstream from the region of interest was suggested for the split/Dirichlet plane. Additionally, the impact of this approach on the aerodynamic coefficients of the EFTV was minimal, less than 1% for all the considered panels.

After the verification study, a numerical analysis was carried out on the detailed configuration using the reduced model approach. This model was created to represent the EFTV flight configuration as closely as possible and including all the necessary geometrical details. The results obtained for these sets of simulations showed that the "original" flight model was susceptible to high-heat transfer regions near the wing-aileron region and the assembly structure. Moreover, the aerodynamic data for the original flight model showed a change in the vehicle pitching moment when compared to the clean AEDB configuration at Mach 7.5 with AoA of 0^0. The impact of the convective heating on the torsion-bar cavity wall and the bearing structure was found to be negligible for low AoAs, but there was increased heating at an AoA of 15^0, but well below the maximum operable temperature for the torsion-bar bearing.

A modified flight configuration was proposed as a part of this study to reduce the local hot spots on the original EFTV flight configuration and to bring the aerodynamic characteristics of the vehicle closer to the nominal model used for the AEDB calculations. This included the closing of wing and aileron cavity gaps. This modified flight model was used to calculate the variations from the AEDB database due to the geometric configuration. The analysis of the data for the modified flight configuration shows that the changes in the aerodynamic characteristics due to the detailed geometrical configuration is less than 5% when compared to the "clean" AEDB model. Although, for an aileron deflection angle ($\delta_{aileron}$) of -15^0, there is a change of about 2^0 for the trim AoA for the EFTV vehicle with the modified model. Moreover, the maximum difference seen in the hinge moment coefficients between the AEDB and modified flight configuration were about 4.7% and 2.95% at Mach 7.5 (AoA = 15^0 and $\delta_{aileron}$ = -15^0) and Mach 4.0 (AoA = 0^0 and $\delta_{aileron}$ = -5^0), respectively for the considered flight cases. The aileron efficiency for the EFTV is reduced by the presence of the hinge line in the modified flight model compared to the AEDB model for the flight Mach number of 7.5.

6. Acknowledgements

This work was performed within the 'High Speed Experimental Fly Vehicles - International' (HEXAFLY-INT) project fostering International Cooperation on Civil High-Speed Air Transport Research. HEXAFLY-INT, coordinated by ESA-ESTEC, is supported by the EU within the 7th Framework Program Theme 7 Transport, Contract no.: ACP3-GA-2014-620327. Further information on HEXAFLY-INT can be found on http://www.esa.int/techresources/hexafly_int.

The first author would like to thank the European Space Agency (ESA) for sponsoring the International Research Fellowship in the framework of international collaboration between ESA and Australia.

References

1. Steelant, J. et al., Numerical and Experimental Research on Aerodynamics of a High-Speed Passenger within the HEXAFLY-INT Project, 30th Congress of the International Council of the Aeronautical Sciences, 2016.
2. Schettino A. Pezzella G., Marini M., Di Benedetto S., Villace V.F., Steelant J., Gubanov A. and Voevodenko N.: Aerodynamic and Aerothermodynamic Database of the HEXAFLY-Int Hypersonic Glider. HiSST: International Conference on High-Speed Vehicle Science Technology, HiSST 2018-2940957, 26–29 November 2018, Moscow, Russia.
3. Steelant J., Marini M., Pezzella G., Reimann B., Chernyshev S.L., Gubanov A.A., Talyzin V.A., Voevodenko N.V., Kukshinov N.V., Prokhorov A.N., Neely A.J, Kennel C., Verstraete D., Buttsworth D., 'Numerical and Experimental Research on Aerodynamics of High-Speed Passenger Vehicle within the HEXAFLY-INT Project', 30th Congress of the International Council of Aeronautical Sciences (ICAS), 25-30/09/2016, Daejeon, Korea.
4. Institute of Aerodynamics and Flow Technology, German Aerospace Center (DLR), The DLR TAU Code, 2012. URL: http://tau.dlr.de/.
5. Wada, Y., Liou, M.S., "A flux splitting scheme with high-resolution and robustness for discontinuities", AIAA Paper 94-0083, 1994.
6. Spalart, P.R., Allmaras, S.R., "A One-Equation Turbulence Model for Aerodynamic Flows", AIAA-92-0439, 1992.